Trends in the erythemal radiant exposure from re-evaluated measurements (1976−2023) with biometers at Belsk, Poland, and their sources from corresponding ozone, aerosol, and cloud observations

Agnieszka Czerwińska[1], Janusz Krzyścin[1], Janusz Jarosławski[1], Piotr S. Sobolewski[1], Aleksander Pietruczuk[1]

[1]Institute of Geophysics, Polish Academy of Sciences, Warsaw, 01-452, Poland

Correspondence to: Agnieszka Czerwińska (aczerwinska@igf.edu.pl)

Abstract. The world's longest homogenised series of measured erythemal solar irradiance comes from biometers operating at Belsk, Poland (51.84° N, 20.79° E) in period 1976−2023. Linear trends in erythemal radiant exposure (ERE) are calculated for the first (1976−1999) and second (2000−2023) halves of the observations. observation period. A statistically significant increasing trend of 6.9% per decade was found for annual ERE in the first period. In the second period, only the trend in seasonal (June-August) ERE was statistically significant (3.1% per decade). The method proposed here to reveal the sources of the ERE trends involves the construction of separate and combined forcings from clear sky (total column ozone and aerosol optical depth) and cloud proxies (sunshine duration, clearness index). The superposition of these proxy effects over 1985−1999 was the source of the positive trend in annual ERE for the first half of the observations. Before 1985, clear sky and cloud effects had cancelled each other. The maximum ERE growth rate of 19.4% per decade over 10 years was found in 1984−1993, with overlapping forcing effects of decreasing ozone and cloudiness responsible. Clear sky and cloud effects stabilised after 1996 and 2005, respectively. The cloud effect has begun to force a positive trend in the annual ERE again since 2015 due to increasing cloud transparency and/or the disappearance of cloud cover. Comparisons of the performance of linear and non-linear versions of the ERE models show that interaction effects between clear sky and cloud proxies can be neglected in trend analyses.

1 Introduction

UV radiation (UVR) passing through the atmosphere is attenuated because of absorption and scattering by gaseous substances (e.g. absorption mainly by O_3, NO_2 and SO_2 in the UV-B region of the solar spectrum, and Rayleigh scattering by atmospheric molecules, with the strongest influence from the most abundant nitrogen and oxygen molecules), aerosols (e.g. absorption by soot particles and Mie scattering by dust particles), and cloud particles (scattering by cloud droplets and ice crystals). The path length of solar radiation to the ground depends on the sun's elevation and the altitude of the site, so the time of day, the day of the year and the geographical coordinates are also important factors in surface UV variability on intraday and seasonal time scales (DeLuisi, 1997).

Studies of changes in surface UVR have usually been combined with analyses of corresponding changes in its forcing factors, such as ozone, aerosols and clouds (e.g. Calbó et al., 2005; Borkowski, 2008; Krzyścin et al., 2011; Fountoulakis et al., 2018; Aun et al., 2019; Bernhard et al., 2023). Excessive UV radiation has been linked to a number of health problems (Neale et al., 2023), such as erythema appearance, skin cancer (including the deadly melanoma), cataracts and immunosuppression (Young, 2006, Bernard et al., 2019). On the other hand, UVR-induced cutaneous synthesis is the main source of vitamin D_3 in the human body (Holick and Chen, 2008). In additions to being the main source of vitamin D, exposure to UVR has other positive effects. E.g.,: lowering the blood pressure, psoriasis clearing, improving mood by endorphin release, and increases the melanin production in skin (Juzeniene and Moan, 2012; Trummer et al., 2016). Since the mid-1980s, there has been interest in changes in erythemal solar radiation at ground level, along with the observed downward trend in stratospheric ozone over Antarctica.

This tendency appeared in the early 1980s as a result of the accumulation of man-made ozone-depleting substances (chlorofluorocarbons) in the stratosphere (Molina and Rowland, 1974; Farman et al.,1985; Solomon et al., 1986).

Erythemal UV irradiance is the intensity of UV radiation that causes sunburn, i.e., UV spectrum weighted with action spectrum of erythema (sunburn) appearance and integrated over the wavelength range from 280 to 400 nm. The commonly used 1 UV Index is equivalent to 25 mW m^{-2} of erythemal UV irradiance (WHO, 2002).

A global erythemal irradiance observing network of about 15 stations, was established in the early 1970s (WMO, 1977). This followed the construction of the Robertson-Berger (RB) meter, which made it possible to monitor erythemal irradiance (Berger, 1976), rather than the recognition of the urgent need for such observations. RB meter was also installed in 1975 at the Central Geophysical Observatory of the Institute of Geophysics (IG), Polish Academy of Sciences (PAS), located at Belsk, i.e., a rural site in central Poland. Regular monitoring has been started here in January 1976 as part of the geophysical monitoring including also parameters important to its variability as total column ozone (TCO$_3$) by the Dobson spectrophotometer, and cloud attenuation of solar radiation by Cambell-Stokes sunshine recorder and global solar irradiance by various pyranometers. Since the early 1990s, other next-generation broadband biometers were used for UV monitoring, including the Solar Light (SL) Model 501 A biometer (#927 and #2011 for the period 1993−1994 and 1995−2013, respectively) and the Kipp & Zonen (KZ) UV-AE-T #30616 from 5 August 2013 to the present. The homogenisation of the 1976−2013 SL time series was performed by comparing the measured erythemal radiant exposure (ERE) under clear skies with the output of the Tropospheric Ultraviolet and Visible (TUV) Radiation Transfer Model (TUV, 2025). The quality of the KZ measurements (2013−2023) was supported by the well-maintained Brewer Mark II #64 spectrophotometer. ~~Therefore, it can be stated that the world's longest homogenised time series of~~The SHICRivm algorithm is used for quality checks and to extend the Brewer spectra to 400 nm (Slaper et al, 1995). To retrieve daily erythemal radiant exposures for comparison with KZ, spectra are weighted with the CIE erythemal action spectrum (CIE 2019) and integrated over wavelengths (from 280 to 400 nm) and time (sunrise to sunset). Time series of UV ground-based measurements longer than four decades are very rare. They are not erythemally weighted (Chubarova et al., 2000) or do not come from biometers, but rather spectral measurements (NDACC, 2025, WOUDC, 2025). Therefore, it can be stated that the world's longest homogenised time series of measured erythema-weighted solar irradiance comes from biometers operating at Belsk (Krzyścin et al., 2025).

This article focuses on the investigation of the long-term variability of monthly, seasonal, and annual ERE and its sources, taking into account the co-observed time series of factors influencing UVR, i.e. TCO$_3$, aerosol optical depth (AOD) and different characteristics (sunshine duration, global solar irradiance, clearness index) of solar radiation attenuation by clouds. The paper is organised as follows. The data used are described in Sect. 2. The trend analyses using standard least squares linear regression are presented in Sect. 3 for the monthly, annual and seasonal (June−August) ERE. Section 4 presents estimates of ERE forcing by individual UVR drivers and their linear and non-linear superposition. Section 5 provides a discussion of the results.

2 Data

In this study, we used the following data collected at Belsk: ERE, TCO$_3$, sunshine duration (SunDur), daily global solar radiant exposure (G) and aerosol optical depth at 340nm (AOD$_{340\,nm}$). The data were archived in the IG Data Portal (Krzyścin, 2024). The instruments used and their operating periods are presented in Table 1.

Table 1. The Belsk instruments that were used in this study and their periods of operation.

Data	Instrument	Operation period
Daily ERE	Robertson Berger Meter (290−350 nm)	1976−1994
	SL Biometer 501 A # 927 (280−400 nm)	1993−1994
	SL Biometer 501 A # 2011 (280−400 nm)	1995−2013
	Kipp-Zonen UV-AE-T # 30616 (280−400 nm)	2014−present
TCO$_3$	Dobson Spectrophotometer # 84	1963−present
SunDur	Campbell–Stokes sunshine recorder	1966−1968, 1970−1973, 1975−now
G	Kipp CM 6, Sonntag PRM-2, Kipp&Zonen CM 11, and Kipp&Zonen CM 21	1966−now
AOD$_{340nm}$	Sonntag pyrheliometers	1976−2013
	CIMEL CE 318-T	2004−now

2.1 Erythemal radiant exposures

Recently, daily ERE from various biometers operated at Belsk over the period 1976−2023 (as shown in Table 1) were homogenised by multiplying the measured (raw) data by the calibration coefficients, obtained as the smoothed ratio between the modelled erythemal irradiance at noon and the corresponding values from measurements on cloudless days. Tropospheric Ultraviolet and Visible (TUV), available from http://acd.ucar.edu/UV/, was used to simulate erythemal irradiances at cloudless noon. TUV was developed by Madronich (1993) and version 5.4 was implemented here (TUV, 2025). Inputs to this model were time, TCO$_3$, AOD$_{340 nm}$, Ångström coefficient α, surface albedo, single scattering albedo and aerosol asymmetry factor. The values of the last four variables were kept constant and equal to climatological values typical for rural sites. The raw, homogenised results from the biometers measurements and corresponding clear sky daily ERE (by TUV model) are available on the IG Data Portal (Krzyścin, 2024). Here, in the case of days with missing UVR measurements, the gaps were filled with the corresponding monthly means of daily ERE (if the number of measurements in the month was not less than 14). If a whole month was missing (December 2014), the value was filled with the long-term monthly mean (2004−2023). The months of 1985 (June and July) were excluded from the analyses because of the lack of data, and replacing them with long-term monthly means seems to be incorrect, as UVR in these months contributes mostly to the annual ERE. The homogenisation procedure of the Belsk UV measurements is described in detail by Krzyścin et al. (2025).

2.2 Ancillary data

Daily TCO$_3$ values are taken from the IG Data Portal. They are marked with quality flags. Flags 1−5 indicate measurements from Dobson spectrophotometer #84 (the most reliable values are marked with flag 1 and refer to direct sun measurements), flags 6−7 are from satellite measurements and flag 8 is from the Modern-Era Retrospective Analysis for Research and Applications version 2 (MERRA-2) database (GMAO, 2025). Dobson results represent more than 90% of the time series. More details can be found in Krzyścin et al. (2015). SunDur has been measured with Campbell-Stokes sunshine recorders since 1966. As a predictor of cloud properties, SunDur is used as a relative value (percentage of daily duration), from sunrise
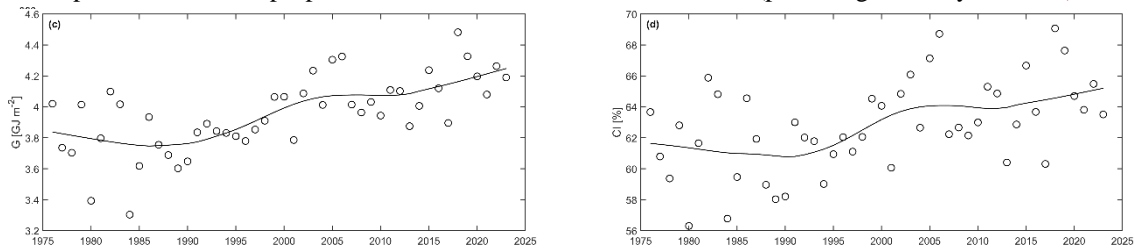
105 to sunset). G has been measured since 1966 with various pyranometers (Table 1) calibrated to the Polish national standard (previously calibrated at the World Radiation Centre in Davos). In the years 1976−2013, $AOD_{340\,nm}$ was obtained from the Linke turbidity factor measurements with Sonntag pyrheliometers (Posyniak et al., 2016), and since 2004 until now it has been measured within the Aerosol Robotic Network (AERONET) (AERONET, 2025) with CIMEL CE 318-T, data level 2.0. The clearness index, (CI), i.e. the quotient of G and G_0 (clear sky value of daily global radiant exposure), was expressed in per cent,

110 with G_0 from the fifth version of the global reanalysis of the European Centre for Medium-Range Weather Forecasts (ERA5, 2025) and (MERRA-2, 2025). For G_0, we compared measured G for cloudless sky conditions at Belsk with G_0 from MERRA-2 and ERA5. We found that the best fit was for the mean values of MERRA-2 and ERA5. Before 1980, we used ERA5, but the data was corrected with the mean bias.
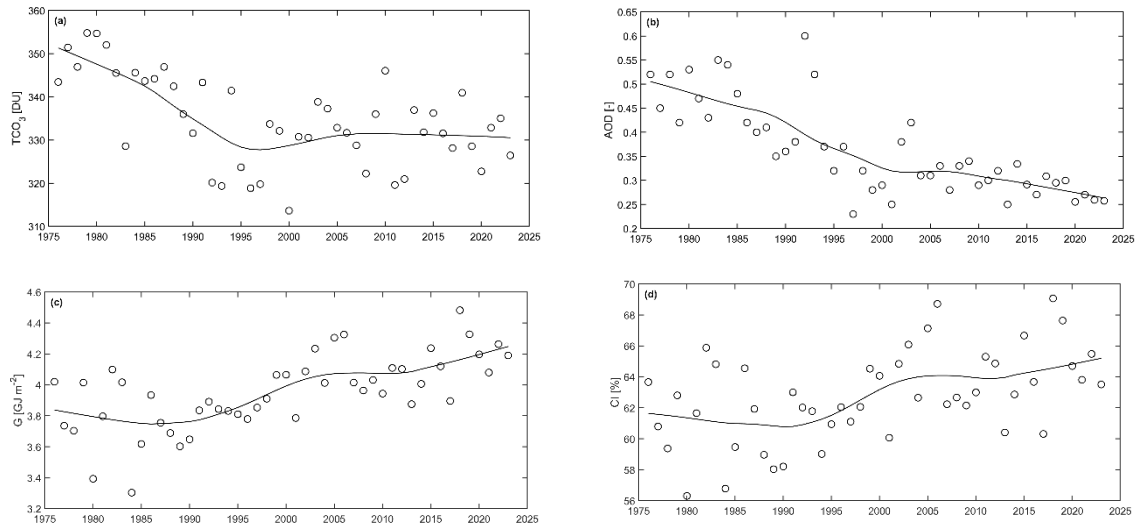
115

Figure 1: The annual 1976−2023 time series of the basic UVR drivers: (a) TCO_3 in Dobson Unit, (b) AOD_{340nm} − dimensionless values, (c) yearly sum of G in GJ m^{-2}, (d) CI (G/G_0) – dimensionless value.

The CI value, which is calculated on the basis of daily ERE, CI_{ERE}, is proportional to the CI value from global solar radiation. The conversion formula is often in the form: $CI_{ERE} = \alpha CI^{\beta}$, where the coefficients are derived empirically and may depend on

120 solar zenith angle, resulting in a smaller CI_{ERE}/CI ratio at lower solar elevation (e.g. Krzyścin et al. 2025). Figure 1 shows the annual means of TCO_3, AOD_{340nm}, CI, and the annual sum of G. These variables are fundamental drivers associated with clear sky (the first two variables) and cloud effects (the last two variables) on UVR. The time series of these drivers show considerable long-term variability. Their impact on monthly and annual ERE is presented later in the text (Sect. 4).

3 Trends in the UV measurements

125 This section presents the long-term variability of monthly, seasonal and annual ERE. Seasonal ERE refers to the summer months of June, July and August, which are the most important for human health, as the intensity of erythemal radiation tends to be high during these months and people spend more time outdoors. Our first guess was that a linear trend for the whole period 1976−2023 would not be applicable because of a trend shift in the annual ERE, somewherevisible in the smoothed data, that occurred between the years 1995−2015. The year 2000 was chosen as the trend-turning year that divided the whole

130 observing period into two sub-periods (1976−1999 and 2000−2023) with equal length, and also to choose the same turning point for each time series. The effect of this selection on the trend values is discussed further in this Section.

The trends, expressed as a percentage of the 20-year average (2004−2023), are shown in Table 2 and Figs. 2−3. A linear trend is considered statistically significant if the doubled standard error (SE) of the slope coefficient is smaller than the absolute

value of the slope. In such a case, the trend is shown in bold. The SE is multiplied by the autocorrelation factor $F =$
135 $\sqrt{1 + R_{k+1})/(1 - R_{k+1})}$ if the autocorrelation coefficient for a time lag of one year, R_{k+1}, is greater than 0 (for $R_{k+1}<0$, $F=1$) (Weatherhead et al. 1998).

In the 1976−1999 sub-period, the positive linear trends were statistically significant in April (5.7% per decade), May (10% per decade), June (5.5% per decade) and July (8.6% per decade). However, in August (7.9% per decade) the trend was significant before adjusting for the 1-year lagged autocorrelation in the trend residuals. The upward seasonal (June−August) and annual
140 trends were statistically significant at 6.9% and 7.4% per decade, respectively. In the 2000−2023 sub-period, only the seasonal trend (3.1% per decade) was statistically significant.
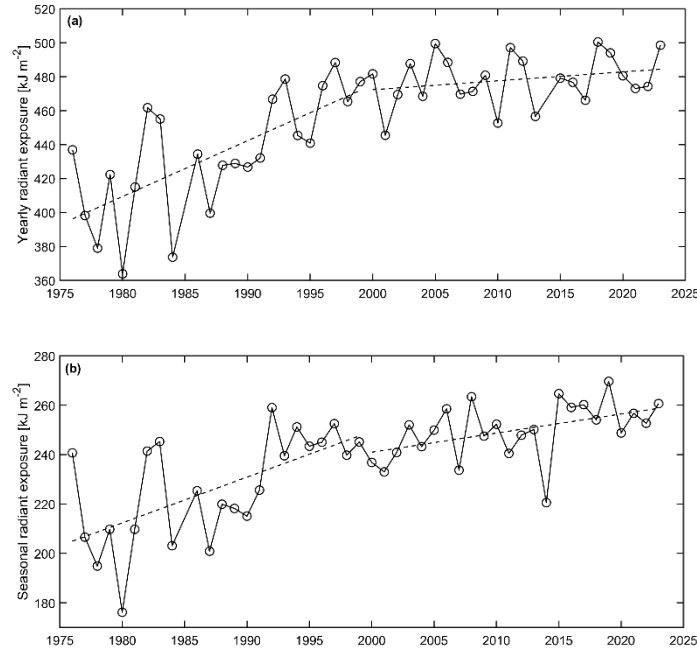
Figure 2. Two disjoined linear regressions (for the 1976−1999 and 2000−2023 period) by the least-squares method applied to: (a)
145 **annual ERE, and (b) seasonal (June−July−August) ERE.**
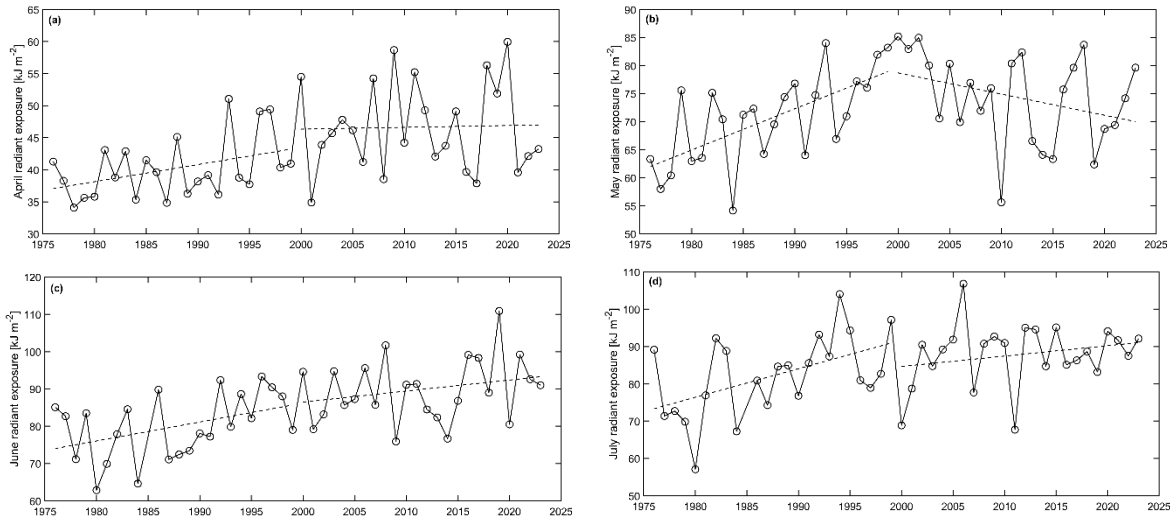
Figure 3. The same as Fig.2 but for the monthly ERE: (a) - April, (b) - May, (c) - June, and (d) July.

In addition, ERE means from the last (2014−2023) and the first (1976−1985) decade of Belsk UVR observations were
150 compared and the significance of the differences between them was checked using a two-sample *t*-test (Table 2). In most cases, the difference was statistically significant (March, April, June, July, August, September, December, seasonal and annual values) and in these cases it exceeded 10%. The ~~large~~largest differences were observed for June (~18%), April (~17%) and

seasonal values (~16%). For annual values, the difference was ~14% and for other months where the difference was statistically significant the difference ranged from ~12% to ~15%. For January, February, May, October and November the difference was

155 not significant and <10%.

Table 2. Linear regression slopes (in % per year) in the first and second halves of the observations for monthly, seasonal (June−August) and annual erythemal radiant exposures with corresponding standard errors (SE$_{corr}$) adjusted for the one-year lagged autocorrelation (R$_{k+1}$) in the exposure time series. Relative difference (RelDiff) between the means for the last decade and the first decade, expressed as a percentage of the mean for the last decade. p-values are from *t*-tests for the difference between means.
160 **Statistically significant results are shown in bold.**

Type of time series	Trends$_{1976–1999}$ [% per yr]		Trends$_{2000–2023}$ [% per yr]		RelDiff	p_Value
	Slope (±SE$_{corr}$)	R$_{k+1}$	Slope (±SE$_{corr}$)	R$_{k+1}$	[%]	
Jan	0.53 (±0.45)	−0.10	0.00 (±0.41)	−0.20	0.57	0.92
Feb	0.04 (±0.44)	−0.36	−0.05 (±0.36)	−0.35	8.24	0.19
Mar	0.74 (±0.43)	0.13	−0.15 (±0.46)	0.26	12.04	**0.03**
Apr	**0.57** (±0.27)	−0.24	0.06 (±0.45)	−0.24	16.58	**0.01**
May	**1.02** (±0.25)	−0.22	−0.52 (±0.33)	0.04	9.16	0.06
Jun	**0.55** (±0.26)	−0.17	0.33 (±0.28)	−0.31	17.97	**<0.01**
Jul	**0.86** (±0.37)	0.16	0.31 (±0.28)	−0.16	14.29	**0.01**
Aug	0.79 (±0.42)	0.36	0.28 (±0.25)	−0.20	14.66	**<0.01**
Sep	0.43 (±0.38)	0.05	0.24 (±0.45)	−0.22	14.30	**0.02**
Oct	−0.06 (±0.34)	−0.12	−0.37 (±0.47)	0.10	2.50	0.70
Nov	0.63 (±0.42)	0.07	0.07 (±0.36)	−0.29	2.95	0.60
Dec	0.68 (±0.35)	−0.00	0.35 (±0.66)	0.12	13.13	**0.02**
Yearly	**0.69** (±0.16)	−0.07	0.09 (±0.11)	0.01	13.84	**<0.01**
Seasonal	**0.74** (±0.24)	0.14	**0.31** (±0.12)	−0.28	15.91	**<0.01**

Independently, we analysed which trend-turning point would provide the best two-line regression fit to the observed ERE time series. We calculated a set of coefficients of determination, R^2_T, using two regression lines for the period 1976−T and T−2023, where T varied year by year from 1995 to 2015, and T_{max} with the maximum R^2 (R^2_{Tmax}) was ~~selected~~calculated. We found that although R^2_{Tmax} is in some cases higher than R^2_{2000}, the difference in R^2 is not larger than 0.09, and for the series with

165 statistically significant trends observed up to 2000, the difference does not exceed 0.05. The results are presented in Table 3.

Table 3. Determination coefficient for two-slope regression with the turning point in 2000 (R$^2_{2000}$) and in T$_{max}$ (R$^2_{Tmax}$) with the best fit to the observed radiant exposure values. T$_{max}$ is selected from the 1995−2015 range.

Type of time series	R$^2_{2000}$	R$^2_{Tmax}$	T$_{max}$
Jan	0.05	0.05	1999
Feb	0.06	0.12	2013
Mar	0.14	0.19	2015
Apr	0.28	0.30	2009
May	0.31	0.36	2004
Jun	0.35	0.39	2009
Jul	0.25	0.28	1996
Aug	0.38	0.39	2002
Sep	0.21	0.30	1997
Oct	0.05	0.08	2015
Nov	0.06	0.10	2002
Dec	0.12	0.18	2006
Yearly	0.65	0.66	1996, 2007
Seasonal	0.56	0.56	1998, 2000

4 Factors affecting UV radiation

Several geophysical parameters characterising the attenuation of sunlight in the atmosphere have been monitored at Belsk in parallel with surface UV radiation measured with broadband biometers. These are: total column ozone, aerosol optical depth (at 340 nm), sunshine duration, and global solar irradiance. The last two parameters are used to derive relative sunshine duration and the clearness index as a percentage of daylight duration and hypothetical global solar irradiance under clear sky conditions, respectively. In addition, synthetic values of daily erythemal radiation exposure under clear sky conditions are calculated using the TUV model.

In this section, time series of monthly and annual ERE from the Belsk observations for the period 1976−2023 and the influence of different factors on UV radiation will be accessed, analysing the relative deviations of the observed and modelled ERE from the reference level, i.e. the averaged values of monthly (Table 4) and annual EREs (477.5 and 684.5 kJ m^{-2} for all sky and clear sky conditions, respectively) for the period 2004−2023. To reveal UV variations caused by a selected proxy and/or group of proxies, models are run with other proxies held at their reference values and only variations in the proxy of interest are allowed.

Table 4. Mean 2004−2023 observed and modelled clear sky (by TUV model) monthly erythemal radiant exposure and corresponding mean values for potential proxies of UV variability including the daily sum of global solar irradiance (G), relative sunshine duration (rSun_Dur, daily sunshine duration in per cent of the day length), and clearness index (CI, daily sum of global solar irradiance in per cent of its synthetic clear sky representative).

Month	UV (kJ m^{-2})	UV_clear (kJ m^{-2})	TCO$_3$ (DU)	AOD −	G (MJ m^{-2})	rSun_Dur (%)	CI (%)
Jan	4.090	6.975	343.8	0.203	2.365	18.67	49.47
Feb	9.030	14.32	361.9	0.247	5.102	29.83	57.60
Mar	24.11	36.67	376.2	0.308	9.619	37.47	63.34
Apr	47.03	68.31	371.9	0.322	15.35	51.74	70.39
May	72.47	105.5	366.2	0.306	19.60	55.24	72.98
Jun	90.26	125.4	340.9	0.315	22.86	61.06	79.32
Jul	89.28	124.7	331.3	0.348	20.70	55.67	75.75
Aug	72.16	99.23	309.4	0.354	17.82	62.40	77.90
Sep	42.04	59.29	295.2	0.303	12.42	49.59	73.38
Oct	18.52	28.27	286.8	0.259	6.718	38.21	63.27
Nov	5.400	10.30	291.5	0.25	2.827	21.73	48.94
Dec	3.109	5.497	301.9	0.195	1.712	15.804	45.44

Table 5 shows the linear trends (1976−1999 and 2000−2023) in the time series of annual and seasonal means for the above-mentioned proxies for the effect of stratospheric ozone, aerosols and clouds on UVR. The negative trends in TCO$_3$ and AOD$_{340\,nm}$ were statistically significant in the first half of the observations for the annual and seasonal ERE, implying a positive trend in UVR. The negative aerosol trend continued in the second half of the observations but was about three times weaker than in the first sub-period. For the cloud effects, the positive trends are only found in the seasonal means for the second half of the observations. However, it will be discussed further in the text (Sect. 4.2) that changes in cloud parameters had a large impact on the UVR at Belsk.

Table 5. The trends from the standard least squares regression of the UVR forcing factors and their standard errors for the periods 1976−1999 and 2000−2023. The statistically significant trends at the 2σ level are shown in bold.

Variable	Trend in % per decade ± 1 SE			
	1976−1999		2000−2023	
	Annual	Seasonal	Annual	Seasonal
TCO$_3$	**−3.7 ± 0.7**	**−3.6 ± 0.6**	0.2 ± 0.7	0.2 ± 0.6
AOD$_{340\,nm}$	**−29.8 ± 9.8**	**−26.3 ± 8.9**	**−9.6 ± 3.7**	2.5 ± 4.1
G	1.0 ± 1.4	1.7 ± 2.2	1.8 ± 1.2	**3.4 ± 1.3**
CI	0.3 ± 1.3	−0.2 ± 2.2	0.7 ± 1.1	**2.6 ± 1.2**

4.1 Clear-sky conditions

A subset of clear sky days in the whole period of Belsk observations was extracted, assuming that the daily sum of total solar irradiance is close to its synthetic clear sky representative, taken from the ERA-5 and MERRA-2 reanalysis (Czerwińska et al., 2024, Krzyścin et al., 2025). It was arbitrarily set that the clearness index for such days should be greater than 95%. Fig. 4 shows a time series of the frequency of occurrence of clear sky days in the warm (April−September) and cold (October−March) sub-period of the year. Clear sky days are about twice as frequent in the former sub-period than in the latter. The pattern of long-term variability is similar in both cases, with a decrease in frequency at the beginning of the series that lasted until about 1990, and a further increase that is stronger in the period 1990−2005 than afterwards.
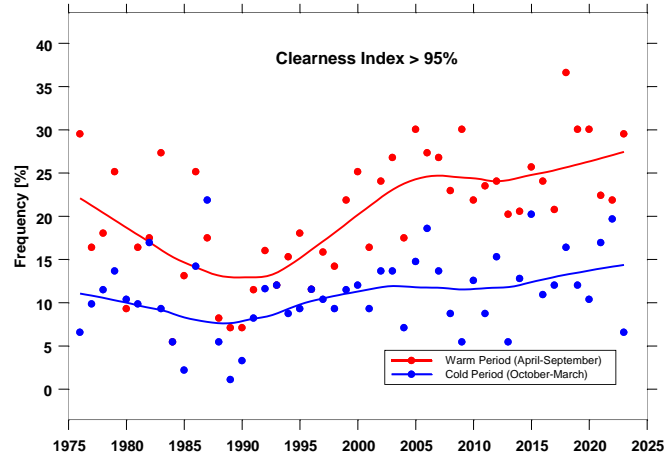
Figure 4. Frequency of clear sky days in the warm (April−September) and cold (October−March) sub-period of the year for the period 1976−2023.

TUV is a radiative transfer model that also provides biologically effective irradiances (here erythemal irradiance) throughout the cloudless day using the following set of input parameters: total column ozone, aerosol optical depth at a selected wavelength, and the Ångström coefficient. Other input parameters are usually set at a fixed level corresponding to typical values for the site. Taking into account climatology of the Belsk's aerosol characteristics (AERONET, 2025) values of 0.95 and 0.69 are taken for single scattering albedo and asymmetry factor, respectively. The Ångström coefficient was chosen to be equal to 0 on the assumption that the AOD values at 340 nm are representative of the whole UV-B range (300−315 nm) and the short wavelength part of the UV-A range. Surface albedo is 0.03 representing a snowless surface covered by grass (Chadyšiene and Girgždys, 2008).

The long-term ozone effect on the clear-sky UV is derived from the version of the TUV model (denoted as TUV_{O3}) with input containing observed TCO_3 values, while all other UV forcing parameters are held constant, with AOD values equal to the monthly mean values calculated over the reference period (Table 4). Similarly, to quantify the aerosol effects, the TUV_{AOD} model takes into account AOD at 340 nm from the measurements, but other input parameters are kept constant. Model TUV_{O3+AOD} calculates the combined effects of ozone and aerosols, assuming that these effects are additive, i.e.,

$$TUV_{O3+AOD} = TUV_{O3}+TUV_{AOD} -TUV_{const} \qquad (1)$$

where TUV_{const} is the TUV version using only constant values (the means for the reference period) for all input parameters. Model (1) is compared to the full TUV model (denoted as $TUV_{O3\&AOD}$) with the observed values of TCO_3 and AOD at 340 nm. The $TUV_{O3\&AOD}$ model may differ from TUV_{O3+AOD} because the former model takes into account possible interactions between ozone and aerosols (e.g. cases with high TCO_3 and low AOD in air coming from the Arctic in early spring), which is neglected in the latter model, which by definition separates ozone effects from the aerosol effects.

Time series by all abovementioned versions of the TUV model are shown in Figure 5. From this Figure, it can be inferred that the long-term ozone and aerosols effects (as shown by the smoothed profiles obtained by LOcally WEighted Scatterplot

Smoothing (LOWESS), Cleveland, 1979) are almost equal providing that the increase in the clear sky erythemal UV is of about 12% in the period 1976−1999. Afterwards, there is no trend in the TUV_{O3} and TUV_{AOD} values providing also trendless pattern of the TUV_{O3+AOD} values.

230
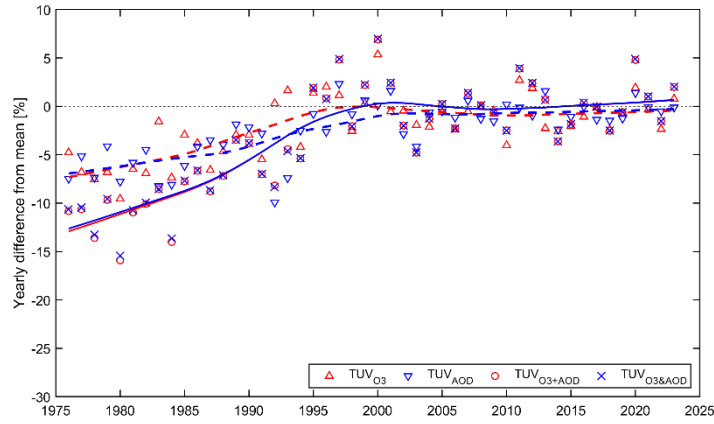
Figure 5. Relative differences of the modelled annual erythemal radiant exposure from the pertaining clear-sky reference value of 684.5 kJ m⁻². The curves show the data smoothed by the LOWESS low-pass filter. The dashed curve and triangles in red refer to the TUV_{O3} model, and the dashed curve and triangles in blue refer to the TUV_{AOD} model. The solid curve and circles in red refer to the TUV_{O3+AOD} model, and the solid curve and crosses in blue refer to the $TUV_{O3\&AOD}$ model.

235   It is worth noting that the long-term pattern of annual EREs by the TUV_{O3+AOD} and $TUV_{O3\&AOD}$ models are close to each other, which means that the effects due to the interaction of these basic clear-sky UV proxies could be omitted from trend analyses. This also makes it possible to construct a simple UV regression model that relates the relative changes in the monthly erythemal exposure from the $TUV_{O3\&AOD}$ model, $\Delta TUV_{O3\&AOD}(i, j)$, to the linear combination of the relative changes in the measured TCO_3 and AOD_{340} nm values:

240   $$\Delta TUV_{O3\&AOD}(i, j) = \alpha_0(j) + \beta_0(j) \times \Delta TCO_3(i, j) + \gamma_0(j) \times \Delta AOD_{340\,nm}(i, j) \qquad (2)$$

where j denotes calendar month and i is the year (i=1976 for the first year of observations and 2023 for the last year). Estimates of the model coefficients with their standard errors are presented in Table 6, together with the standard deviation of the regression model residuals and the coefficients of determination (the squared value of the correlation coefficient between model (2) and $TUV_{O3\&AOD}$).

245   **Table 6. Regression coefficients of the model (2) and their standard errors (SE) for calendar months. Corresponding standard deviation (SD) of the differences and squared correlation coefficient (R^2) between model (2) and $TUV_{O3\&AOD}$ (TUV model using measured TCO_3 and $AOD_{340\,nm}$) values. Value in bold indicates statistically significant value at 2SE level. Dimensionless values are denoted as (−).**

Month	$\alpha_0 \pm$ SE (%)	$\beta_0 \pm$ SE (−)	$\gamma_0 \pm$ SE (−)	SD (%)	R^2 (−)
Jan	**1.112 ± 0.372**	**−0.831 ± 0.033**	**−0.084 ± 0.004**	1.580	0.9597
Feb	**2.749 ± 0.369**	**−0.966 ± 0.036**	**−0.109 ± 0.006**	1.740	0.9640
Mar	0.389 ± 0.231	**−1.032 ± 0.036**	**−0.122 ± 0.006**	1.335	0.9698
Apr	−0.116 ± 0.183	**−1.082 ± 0.033**	**−0.115 ± 0.006**	1.107	0.9812
May	**−0.940 ± 0.105**	**−1.103 ± 0.022**	**−0.098 ± 0.003**	0.594	0.9915
Jun	**0.311 ± 0.072**	**−1.076 ± 0.020**	**−0.096 ± 0.003**	0.416	0.9956
Jul	**−0.806 ± 0.071**	**−1.045 ± 0.021**	**−0.108 ± 0.003**	0.457	0.9933
Aug	**−0.299 ± 0.109**	**−1.062 ± 0.028**	**−0.121 ± 0.004**	0.654	0.9883
Sep	0.121 ± 0.130	**−1.041 ± 0.030**	**−0.110 ± 0.003**	0.737	0.9849
Oct	**0.844 ± 0.279**	**−0.952 ± 0.056**	**−0.094 ± 0.005**	1.367	0.9494
Nov	**0.678 ± 0.302**	**−0.874 ± 0.056**	**−0.099 ± 0.005**	1.433	0.9374
Dec	**1.917 ± 0.280**	**−0.842 ± 0.027**	**−0.071 ± 0.003**	1.143	0.9809

250 The results presented in Table 6 confirm that the linear regression of monthly ERE on TCO_3 and $AOD_{340\,nm}$ is in perfect agreement with the $TUV_{O3\&AOD}$ model, as all monthly coefficients of determination are above 95% and for the spring and summer months this coefficient is even above 98%. It can also be seen that under cloudless sky conditions in the warm (snow-free) season, a 1% decrease (increase) in TCO_3 results in a ~1% increase (decrease) in erythemal radiation exposure. Correspondingly, this rate is about 10 times smaller for changes in $AOD_{340\,nm}$. Slightly lower, but still statistically significant,

255 rates occur during the cold season. These estimates are consistent with earlier findings by Krzyścin and Puchalski (1998).

4.2 All-sky conditions

4.2.1 Non-linear model

The machine learning (ML) approach is implemented to model daily EREs as a function of all available proxies of the surface UVR which have been ~~monitoring~~monitored at Belsk since 1 January 1976 including TCO_3, $AOD_{340\,nm}$, relative daily sunshine

260 duration (SunDur) in per cent of the day length, the daily sum of global solar irradiance (G), clearness index (CI i.e., relative G in per cent of its clear sky representative). These proxies together with measured ERE are archived in the IGF PAS data portal (Krzyścin, 2024).

The ML models were trained using the Regression Learner App in Matlab version 2018a (https://www.mathworks.com/help/stats/regressionlearner-app.html). This tool allows multiple regression models to be

265 trained, their validation errors compared and the best fit selected. The regression models available in this version are: linear regression models (linear, interaction linear, robust linear, stepwise linear), regression trees (fine tree, medium tree, coarse tree), support vector machines (linear, quadratic, cubic, fine Gaussian, medium Gaussian, coarse Gaussian), ensemble of trees (boosted and bagged) and Gaussian Process Regression (GPR) models (rational quadratic, squared exponential, maternal 5/2 and exponential). GPR models are non-parametric, probabilistic and kernel-based. These types of models use a probability

270 over a space of functions as an answer. In the Regression Learner App, the flexibility of the presets is automatically chosen to give the smallest error. Using this approach, we select two GPR models from all available models for further calculations. The best fit for all predictors was a GPR model with an exponential kernel function (which determines the correlation in the response), while in the model with a limited number of predictors (TCO_3, G and relative SunDur) the best fit was GPR with a maternal 5/2 kernel function. Other parameters (kernel mode, sigma mode and base function) were automatically set to

275 optimise the model.

Further in the text, the model built from all available daily values of the proxies will be denoted as GPR_{all}. In addition, the various output of the GPR_{all} model will be examined using:

- GPR_{const} with all proxies fixed to their daily means for the period 2004−2023
- GPR_{clear} with daily values of TCO_3, $AOD_{340\,nm}$. Other proxies are fixed to the daily means for the period 2004−2023

280 - GPR_{cloud} with daily values of relative SunDur, G, CI. Other proxies are fixed to the daily means for the period 2004−2023
- $GPR_{clear+cloud} = GPR_{clear} + GPR_{cloud} - GPR_{const}$

Model GPR_{clear} is for searching a contribution of combined effects of clear sky proxies on the measured daily ERE whereas GPR_{cloud} is for combined effects due to the cloud proxies. The comparison of $GPR_{clear+cloud}$ and GPR_{all} allows us to see if the

285 effects of ozone and aerosols can be separated from the effects of clouds (i.e. the interaction between these groups of variables can be ignored) when discussing the sources of monthly and annual ERE variability.

A version of the GPR model using a limited number of proxies, $GPR_{TCO3* \& SunDur \&G}$, is also constructed, using TCO_3 values from Multi Sensor Reanalysis version 2 (van der A, 2015), hereafter referred to as TCO_{3*}, and only two cloud characteristics of clouds (SunDur and G) from the measurements at Belsk. $GPR_{TCO3* \& SunDur \&G}$ is to reveal a loss of the ML model accuracy

290 when the limited number of proxies is only available from daily monitoring. For a weather station equipped with a Campbell-Stokes recorder and pyranometer, this UV proxy set may be available.

The performance of the most (GPR_{all}) and least ($GPR_{TCO3* \& SunDur \& G}$) extended models is shown in Table 7. The typical descriptive statistics are taken into account: mean relative error (MRE), mean absolute error (MAE), root mean square error (RMSE), and standard deviation (SD) of the relative differences (in per cent of the observed values) between modelled and observed values, and R denotes the Pearson's correlation coefficient between these values. Formal definitions of the statistics can be found in our recent paper (Krzyścin et al., 2025).

Table 7. Descriptive statistics of the most (GPR_{ALL}) and least ($GPR_{TCO3* \& SunDur \& G}$) extended GPR model calculated using the data collected over the period 1976−2023.

Month	GPR_{ALL}					$GPR_{TCO3* \& SunDur \& G}$				
	MRE [%]	MAE [%]	RMSE [%]	SD [%]	R	MRE [%]	MAE [%]	RMSE [%]	SD [%]	R
Jan	−0.05	2.24	2.88	2.91	0.98	−0.33	4.21	5.50	5.55	0.93
Feb	−0.49	2.36	3.46	3.47	0.97	−0.62	3.80	5.43	5.45	0.93
Mar	−0.62	2.26	5.10	5.11	0.96	−0.64	3.17	6.29	6.32	0.94
Apr	0.14	0.98	1.40	1.40	>0.99	0.21	1.28	1.69	1.69	0.99
May	−0.04	1.17	1.56	1.58	>0.99	−0.07	1.81	2.40	2.42	0.98
Jun	−0.04	1.22	1.64	1.65	>0.99	−0.07	1.91	2.60	2.63	0.98
Jul	0.02	1.31	1.73	1.75	>0.99	0.02	2.07	2.71	2.74	0.98
Aug	−0.26	1.66	2.96	2.98	0.98	−0.44	2.75	4.18	4.20	0.95
Sep	−0.13	1.22	1.56	1.57	>0.99	−0.18	2.12	2.70	2.72	0.99
Oct	0.19	1.45	1.82	1.83	>0.99	0.19	2.48	2.95	2.97	0.98
Nov	−0.70	2.11	3.53	3.50	0.97	−0.70	3.60	5.91	5.94	0.92
Dec	0.42	3.31	4.80	4.84	0.95	0.42	6.25	8.50	8.59	0.79

The performance of the two models is very similar, as shown by the small differences in the descriptive statistics, especially in the warm subperiod of the year, where the SD and MAE are only about 1−1.5 per cent point (%p) higher for the version of the model with the fewest proxies. For both models, the model-observation correlation coefficients are very high, exceeding 0.94 for all monthly data within the warm period. In April, the performance of the two models is only slightly different. The difference is less than 0.3 %p. Larger differences are found in the cold season, especially in December, when the SD and MAE of the least extended GPR model are about 5 and 3 %p higher than for the GPR_{ALL} model using all available proxies.

For all GPR models, the monthly sums of the daily ERE are calculated and expressed as relative differences from the monthly 2004−2023 references of the ERE (Table 4). The annual EREs are calculated by adding the monthly sums, which are finally expressed as relative differences from the annual reference of 477.5 kJ m^{-2}. Fig. 6 shows the 1976−2023 time series of the relative differences in ~~the~~ per cent of the annual ERE reference for the observed and set of modelled GPR (GPR_{clear}, GPR_{cloud}, $GPR_{clear+cloud}$, and GPR_{all}).

Analysing the long-term variability in these time series, it can be seen that the annual ERE increases by about 15% in the period 1976−2023, i.e. close to the rate found in the synthetic clear-sky data (Fig. 5). This increase is due to the linear superposition of the ozone and aerosols (GPR_{clear}) and cloud (GPR_{cloud}) effects, as the smoothed $GPR_{clear+cloud}$ time series differs only slightly from the smoothed annual ERE time series based on measurements, which is in perfect agreement with that from the full GPR model (GPR_{all}). The forcing effects of combined ozone ~~&~~and aerosols ~~and~~impact with clouds cancelled each other out at the beginning of the observations, but from about 1986, they started to act in a unidirectional way, causing a fast increase that stopped around 2000. The combined ozone ~~&~~and aerosols effect levelled off a few years before 2000, but the cloud effect levelled off a few years after 2000. Subsequently (around 2010−2015), cloud forcing caused the upward trend to reappear around 2010−2015, but the rate of increase is rather small, comparable to that seen in the 1980s and 1990s. This pattern of long-term changes is generally consistent with that found in the smoothed time series of the observed and GPR_{all} data. However, a complete compensation of the ozone & aerosols and cloud effects found in $GPR_{clear+cloud}$, which occurred until

about 1986, is not supported by GPR_{all} and observed data, as they rather show a slight increase in the annual ERE during this period.
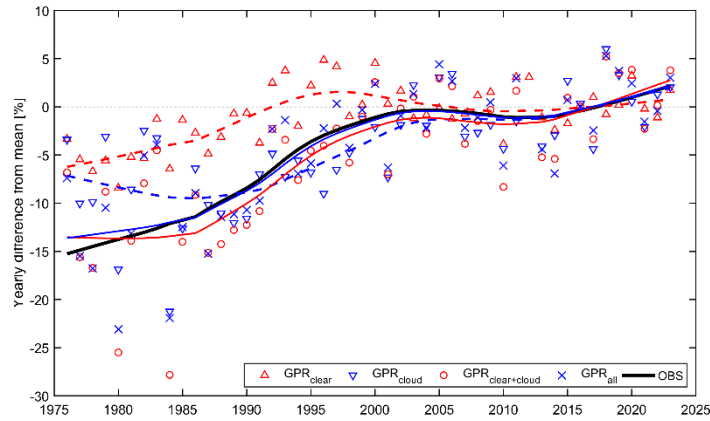
Figure 6. Relative differences of annual erythemal radiant exposures from the 2004−2023 reference for the observed (black solid curve) data and modelled by various versions of the GPR model: GPR_{clear} (dashed curve and triangle up in red), GPR_{cloud} (dashed curve and triangle down in blue), $GPR_{clear+cloud}$ (solid curve and open circles in red), and GPR_{all} (solid curve and crosses in blue). The curves show the data smoothed by a LOWESS low-pass filter.

Figure 7 shows the long-term variability of the annual ERE by the four time series taken from $GPR_{TCO3* \& SunDur \&G}$ output (GPR_{TCO3*}, $GPR_{SunDur*G}$, $GPR_{TCO3*+SunDur*G}$, and $GPR_{TCO3* \& SunDur \&G}$) that corresponds to the four time series by the most advanced GPR_{all} model (GPR_{clear}, GPR_{cloud}, $GPR_{clear+cloud}$, and GPR_{all}). The $GPR_{TCO3* \& SunDur \&G}$ model is for annual ERE estimates for a station with low-cost equipment, i.e. a pyranometer and a Campbell-Stokes instrument, as TCO_3 comes from satellite observations, which is indicated by an asterisk after TCO_3. It can be seen that the long term patterns shown in Fig.6 are almost reproduced, but the $GPR_{TCO3* \& SunDur \&G}$ model gave only slightly larger (lower) differences between the observations up to about 1985 (from 1985 up to 2005−2010).
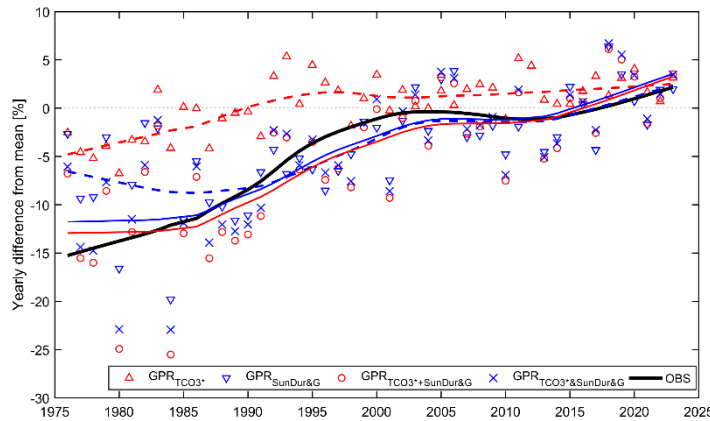
Figure 7. Relative differences of annual erythemal radiant exposures from the 2004−2023 reference for the observed (black solid curve) data and modelled by four versions of the $GPR_{TCO3* \& SunDur \&G}$ output: GPR_{TO3*} (dashed curve and triangle up in red), $GPR_{SunDur\&G}$ (dashed curve and triangle down in blue), $GPR_{TCO3*+SunDur\&G}$ (solid curve and open circles in red), and $GPR_{TCO3*\&SunDur\&G}$ (solid curve and crosses in blue). The curves show the data smoothed by a LOWESS low-pass filter.

4.2.2 Linear regression model

To calculate the direct UV response to the basic forcing factors (TCO_3, aerosols, and clouds), a standard linear regression (*SLR)* of the observed monthly ERE on only two proxies is examined further in this section, i.e. $TUV_{O3\&AOD}$ (clear-sky representative of UV radiation by the TUV model using observed values of TCO_3 and $AOD_{340 nm}$) and CI. The former proxy is intended to account for clear sky effects and the latter for the cloud effects on all-sky monthly ERE over the whole period

(1976−2023) of the UVR observations at Belsk. Further, this model is denoted as $SLR_{clear\&cloud}$ and uses the fractional deviations

of TUV$_{O3\&AOD}$ and CI from the references (shown in Table 1) as the explaining variables:

$$\Delta SLR_{clear\&cloud}(i, j) = \alpha_1(j) + \beta_1(j) \times \Delta TUV_{O3\&AOD}(i, j) + \gamma_1(j) \times \Delta CI(i, j) \tag{3}$$

Table 8. Regression coefficients of the model (3) and their standard errors (SE) for calendar months. Corresponding standard deviation (SD) of the differences and squared correlation coefficient (R^2) between model (3) and the monthly ERE from the measurements. Bolded values indicate a statistically significant regression coefficient at the 2SE level. Dimensionless values are denoted as (−).

Month	$\alpha_1 \pm SE$ (%)	$\beta_1 \pm SE$ (−)	$\gamma_1 \pm SE$ (−)	$\gamma_1 \beta_1^{-1}$ (−)	SD (%)	R^2 (−)
Jan	-1.684 ± 1.507	**0.354 ± 0.168**	**0.729 ± 0.085**	2.06	8.851	0.6450
Feb	2.227 ± 1.343	**0.635 ± 0.136**	**0.754 ± 0.095**	1.19	8.324	0.6410
Mar	0.844 ± 0.973	**0.701 ± 0.122**	**0.763 ± 0.073**	1.09	6.213	0.7800
Apr	0.357 ± 0.604	**0.782 ± 0.073**	**0.820 ± 0.047**	1.05	3.591	0.9400
May	**2.348 ± 0.566**	**0.827 ± 0.084**	**0.871 ± 0.054**	1.05	3.589	0.9030
Jun	**2.964 ± 0.727**	**0.669 ± 0.094**	**0.842 ± 0.058**	1.26	3.772	0.8860
Jul	-0.193 ± 0.610	**0.634 ± 0.103**	**0.778 ± 0.048**	1.23	3.675	0.8960
Aug	0.868 ± 0.771	**0.878 ± 0.116**	**0.847 ± 0.079**	0.96	4.496	0.8440
Sep	0.716 ± 0.710	**0.723 ± 0.121**	**0.813 ± 0.049**	1.12	4.109	0.9280
Oct	0.273 ± 0.836	**0.359 ± 0.140**	**0.720 ± 0.055**	2.01	5.207	0.8450
Nov	**4.060 ± 1.279**	**0.465 ± 0.213**	**0.653 ± 0.085**	1.40	7.772	0.6470
Dec	-1.373 ± 2.283	**0.933 ± 0.234**	**0.433 ± 0.106**	0.46	12.530	0.4860

The regression constants by the least-squares approach are shown in Table 8. The determination coefficients (R^2) are high (~(approximately 0.8= to 0.9) in the March−October sub-period of the year. Thus, the annual ERE can be also correctly estimated as these months contribute to ~95% per cent of the annual ERE. The highest and lowest R^2 values of 0.94 and 0.49 are in April and December, respectively. In addition, it is worth mentioning that in the warm period of the year, the rates of change in the monthly ERE due to 1% change in the explaining variables are almost equal (i.e. $\gamma_1 \beta_1^{-1}$ ~1) and in the ranges (0.63−0.88) and (0.78−0.87) for the clear and cloud effects, respectively.

Having values of the regression coefficients, it will be easy to separate the clear sky effects from the cloud effects using the truncated versions of the model (3), which follow the previous concept (applied to the GPR$_{all}$ model) of allowing variations in one variable but keeping fixed values for other variables:

$$\Delta SLR_{const}(i, j) = \alpha_1(j) \tag{4}$$

$$\Delta SLR_{clear}(i, j) = \alpha_1(j) + \beta_1(j) \times \Delta TUV_{O3\&AOD}(i, j) \tag{5}$$

$$\Delta SLR_{cloud}(i, j) = \alpha_1(j) + \gamma_1(j) \times \Delta CI(i, j) \tag{6}$$

$$\Delta SLR_{clear+cloud} = \Delta SLR_{clear} + \Delta SLR_{cloud} - \Delta SLR_{const} \tag{7}$$

Here, from the definition of the linear model, $SLR_{clear \& cloud} = SLR_{clear+Cloud}$.

365 The pattern of long-term UV forcing variability shown in Fig. 8 is in general agreement with that obtained by the most and least advanced GPR models, as shown in Figs. 6 and 7, respectively. The cloud effects are underestimated in the model (3), ranging from −2% to −5% over the period 1976−1990, while the corresponding change in the GPR$_{all}$ model is −6% to −10%. There is less agreement between the results of model (3) and the observations, as indicated by the larger SD values in Table 8 compared to the corresponding values in Table 7. The long-term pattern of annual ERE from the model (3) starts to correspond

370 exactly to measurements from about 2000−2005 onwards (similarly to that from the less advanced GPR model, Fig.7), but this happened earlier (~1985) in GPR$_{all}$ model (Fig.6).
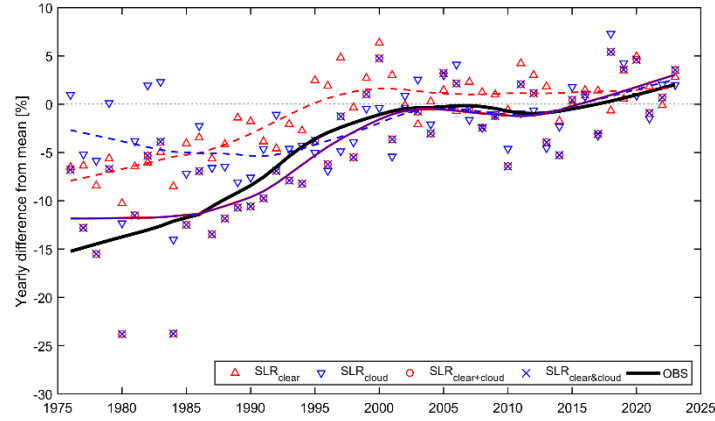
Figure 8. Similar to Fig.6 but time series show various versions of the standard linear regression (SLR) using the clear-sky ERE and clearness index as the explaining variables.

375 **4.2.3 Ranking of the drivers in the annual exposure models**

The ERE drivers in the model discussed in Sect.4 are divided into two categories, i.e. TCO$_3$ and AOD$_{340\,nm}$ for the clear sky cases simulated by the TUV model, and cloud (SunDur, G, and CI) drivers for all sky cases considered in the advanced, simplified GPR, and SLR model. To compare the effects of selected drivers of ERE, the strength coefficient of driver X in a model MOD (SC_MOD$_X$) is proposed as the square root of the mean square of the differences between MOD$_x$ and MOD$_{const}$

380 values. Namely, the X factor can be "clear" and "cloud" in the GPR model for the all-sky ERE (Sect.4.2.1) but "TCO$_3$" and "AOD" in the TUV model for the clear-sky ERE (Sect.4.1). Table 9 shows SC_MOD$_X$ values for all models and individual drivers used in Sect. 4.

385

Table 9. Strength coefficients (SC_MOD$_X$) of the X drivers in the MOD$_x$ model of the annual ERE and their ratios between the second and first driver for the following pairs: X= {AOD, TCO$_3$}, {Clear, Cloud}, {TCO$_3$, SunDur&G}, and {Clear, Cloud} for the TUV, advanced GPR, simplified GPR, and SLR model, respectively. The ratio is between the second and first value from each pair.
390 **The SC_MOD$_X$ is in per cent of the annual reference value (i.e. 684.5 kJ m^{-2} and 477.5 kJ m^{-2}, for the TUV and all-sky models, respectively). The results are for the 1976−2023, 1976−1999, and 2000−2023 period.**

						MOD$_x$					
TUV$_{AOD}$	TUV$_{TCO3}$	ratio	GPR$_{Clear}$	GPR$_{Cloud}$	ratio	GPR$_{TCO3}$	GPR$_{SunDur\&G}$	ratio	SLR$_{clear}$	SLR$_{Cloud}$	ratio
						1976−2023					
3.19	3.24	1.01	4.52	8.75	1.93	3.09	7.81	2.53	4.52	5.48	1.21
	~~Ratio=1.01~~			~~Ratio=~~			~~Ratio=~~			~~Ratio=~~	
						1976−1999					
4.26	4.03	0.95	5.72	11.47	2.00	4.08	10.21	2.50	6.07	7.01	1.16
	~~Ratio=0.95~~			~~Ratio=~~			~~Ratio=~~			~~Ratio=~~	
						2000−2023					

1.52	2.17	1.43	2.86	4.38	1.53	1.59	3.97	2.50	2.01	3.30	1.64
Ratio=1.43			Ratio=			Ratio=			Ratio=		

The effect of the aerosol driver is as strong as that of the ozone driver for the sub-period 1976−1999 and for the whole period 1976−2023. The ozone driver dominates the aerosol driver in the last sub-period 2000−2023 (see the ratio of 1.43 in Table 9). The effects of the cloudy drivers in both GPR models are stronger than the clear sky drivers for the sub-periods 1976−1999, 2000−2023 and for the whole period 1976−2023 (the ratios are in the range [1.5, 2.5]). The same patterns are observed for the SLR drivers in the sub-periods 1976−1999, 2000−2023 and for the whole period 1976−2023, but the dominance of the cloud driver is less evident with the strength coefficients in the range [1.2, 1.6].

5 Discussion

In Europe, UVR measurements mainly come from broadband instruments, which are grouped in national UV monitoring networks to inform the public about the danger of strong UVR through a UV index (Schmalwieser et al., 2017). This is also the case in Poland, where there are several stations with regular UVR monitoring. Among them, Belsk has the longest time series (4748 years) (Krzyścin et al., 2025). The previous trend analysis of the Belsk 1976−2008 UVR data showed a statistically significant increase in annual ERE of $5.6 \pm 0.9\%$ per decade for this period (Krzyścin et al., 2011). Using reconstructed annual ERE based on statistical models, den Outer et al. (2010) calculated trends of 5.2 ± 1.3 and $5.8 \pm 1.5\%$ per decade at Hradec Kralove (50.2° N, 15.8° E), Czech Republic and Lindenberg (52.2° N, 14.1° E), Germany, respectively, for the period 1980−2006. The trend analyses at thethese neighbouring stations of Belsk showed a slightly less positive trend than the present estimate of $6.9 \pm 1.6\%$ per decade for the period 1976−1999. Such a difference seems to be a local effect, not caused by the different periods used for trend estimations, as the trend at Belsk calculated exactly for the period 1980−2006 was $7.0 \pm 1.2\%$ per decade, i.e. almost the same as for the period 1976−1999. Fountoulakis et al. (2020) found that local effects mainly related to the aerosolschanges in aerosol load, albedo, and cloud cover changes in Europe, were important in shaping the UVR trend. In the case of Reading (51.4° N, 0.9° W), UK, and Sodankylä (67.4° N, 26.6° E), Finland, downward trends in the 307.5nm irradiance were even found between 1996 and 2017. In Central Spain, Bilbao et al. (2011), based on a reconstructed series of the erythemal irradiance, recorded upward trends of 3.5% and 4.1% per decade for summer and autumn in the period 1991−2010.

For the shorter period in the 1980s and 1990s, the annual ERE trend was even much larger. From the reconstructed daily ERE, Čížková et al. (2018) calculated trends in successive decades (1964−1973, 1974−1983, 1984−1993, 1994−2003, 2004−2013) and only the 1984−1993 trend appeared statistically significant at $14.9 \pm 6.1\%$ per decade. The corresponding trend at Belsk was found to be also slightly higher at $19.4 \pm 4.2\%$ per decade. Such a strong trend between 1984 and 1993 was due to the overlapping clear sky and cloud effects, both of which caused UVR to increase (Figs. 6−7).

UVR measurements at stations in Central and Eastern Europe have not shown statistically significant annual ERE trends in the current century, including at Moscow (55.8° N, 37.9° E), Russia, in the period 1999−2015 (Chubarova et al., 2018), and at Tõravere (58.37° N, 26.5° E), Estonia, in the period 2004−2016 (Aun et al., 2019). This disappearance of the trend was due to the lack of trends in the main UV forcing factors, i.e. TCO_3, AOD and G. The same trendless pattern of annual ERE was found at Belsk without trends in these forcing factors since 2000 (Table 5). Zerefos et al. (2012), who analysed the long-term variability of UV solar irradiances at 305 nm and 325 nm over selected sites in Canada, Europe and Japan, pointed out that for all of these sites, the trendless period began around 2007. However, the continuation of the upward trend ($3.1 \pm 1.2\%$ per decade) since 2000 was found in Belsk only in the seasonal (June−August) ERE due to lower attenuation of downward solar radiation, as the positive trends in G and CI were statistically significant at $3.4 \pm 1.3\%$ and $2.6 \pm 1.2\%$ per decade for the period 2000−2023. In addition, the frequency of days with clear skies (i.e. higher G) increased during this period (Fig. 4).

~~There is general agreement that stratospheric ozone, aerosols and clouds are the main forcing factors on surface UV (e.g. Fountoulakis et al., 2018; Bernhard et al., 2023).~~ The idea behind the proposed method to identify the long-term variability sources~~This paper proposes a method to reveal the sources of long-term variability and the strength of the induced UVR variability due to individual forcing factors. The idea behind this method~~ is to construct an individual time series of ERE due to each selected proxy (or set of proxies), holding other proxies at their reference levels (means for the last 20 years). ~~The linear and non-linear superposition of clear sky and cloud effects are also calculated and compared with each other and with observations.~~ Using this method, it was found that superimposed clear sky and cloud proxy effects between 1985 and 1999 were the source of the positive trend in annual ERE in the first half of the observations (Fig. 6). Prior to 1985, clear sky and cloud effects almost cancelled each other out. The clear sky and cloud effects stabilised after about 1996 and 2005 respectively, but the latter proxy seems to force a positive trend in the annual ERE again since about 2015 due to increasing cloud transparency. This conclusion aligns with other studies. Fountoulakis et al. (2021) found that in 2006-2020, the levels of UV irradiance at Aosta, Rome and Lampedusa (Italy) increased mainly due to changes in cloud clouds or/and aerosol. Lorenz et al. (2024) also attribute the increasing trend in erythemal UV radiation in Dortmund (Germany) in 1997-2022 to a change in cloud cover as the primary driver. In the reconstructed series in Novi Sad (Serbia) in 1971-2018, Malinović-Milićević et al. (2022) found that there were no significant trends in the last two decades, but there was an increase in the number of days with high daily radiant exposures. The authors also stated that the cloud cover had more influence than TCO_3.

The uncertainty of the homogenisation procedure can be assessed by comparing the descriptive statistics of the differences between the regression model and the observed daily EREs from the KZ meter (operated at Belsk from 2014 to the present day with no required adjustments, as evidenced by the excellent agreement with co-located Brewer spectrophotometer observations; Krzyścin et al., 2025) with the corresponding statistics of the model-observation differences using the homogenised RB and SL501A measurements (1976–1992 and 1993–2013, respectively). The model was trained using data from 2014 to 2023 and applied to pre-2014 periods. For full-year data, the mean relative difference between the model and the KZ observations is 1.4%, whereas it is between −2.7% and 1.6% for the RB and SL501A meters, respectively. The respective standard deviations were found to be 10.4%, 13%, and 14.6% (see Table 4 in Krzyścin et al., 2025). These descriptive statistics are only a few percentage points higher than those obtained for the KZ measurements. Thus, the homogenisation procedure for the period 1976–2013 resulted in a slight increase in uncertainty due to differences in the individual instrumental characteristics of the RB and SL501A meters, as well as the limited aerosol input data (annual mean AOD) used in the regression model, which was derived from sparse Sonntag pyrheliometer measurements in that period.

The strength coefficient (SC_MOD_X) of the selected X driver effect on the annual ERE obtained with each of the models considered here (i.e. the TUV model, the advanced and simplified GPR model, and the SLR model) is proposed to establish a ranking of the drivers. A strong dominance of cloud driver appeared for GPR models as the ratios between SC_MOD_X values are in the range of 1.5−2.5. This dominance is not so apparent for SLR models, where the ratios are ~1 in the range of 0.85−1.64 (Table 9). In the case of the TUV model, the effects of TCO_3 and aerosols are almost equal for the whole UVR observation period and for the period 1976-1999, as the ratio between the respective strength coefficients is ~ 1. The dominance of the TCO_3 effect was found in the period 2000-2023 with a ratio of 1.43, which corresponds to the cleaning of the atmosphere over Belsk in connection with a European-wide policy to improve air quality.

A comparison of linear and non-linear superposition of the effects induced by clear sky and cloud proxies shows the importance of non-linear interactions between these proxies in producing the long-term changes of ERE. A measure, the interaction strength coefficient (ISC), is proposed to assess the strength of such interactions. This is defined as the square root of the mean square of the difference between the linear and non-linear model values, ~~i.e. between~~represented by the red circles and blue crosses in Fig. 6 and Fig. 7. For these Figures, small ISC values of 1.53% and 0.84%, respectively, are calculated, which means that the interaction effect between clear sky and cloud proxies can be neglected in trend analyses, which is also supported by a close similarity in the smoothed ERE patterns with the linear and non-linear model. It is also found that the non-linear

interaction between the effects of TCO_3 and $AOD_{340\ nm}$ on ERE for cloudless conditions gives ISC of 0.13%, meaning that the simple linear model (2) can replace the time-consuming simulations of the TUV model (Fig. 5).

At first glance, the proposed indices to explain changes in annual and seasonal (summer) erythema exposure appear to be only loosely related to the UV radiation attenuation in the atmosphere. To account for the effect of aerosols, the daily averaged $AOD_{340\ nm}$ was used with an Ångström exponent of 0 across the UV range, while other features were held constant. SunDur, G and CI (i.e. parameters related to global solar radiation rather than UV radiation) were chosen to account for the influence of clouds. In addition, a constant surface albedo of 0.03 was used throughout the year. However, this choice of UV indices ensured excellent agreement between modelled and observed annual ERE, as shown in Fig.6 where the smoothed modelled (GPR_{all}, blue solid curve) and observed (black solid curve) curves were almost superimposed on each other. The descriptive statistics of the relative differences between the model and observations are −0.04%, 0.89%, 0.98 and 1.25% for mean, mean absolute value, correlation coefficient and standard deviation, respectively. These values also confirm the effectiveness of using a limited number of proxies in analyses of long-term variability in surface UV radiation. Small differences in the long-term patterns of the annual ERE with the model using a full set explaining variables (GPR_{all}) and model ($GPR_{TCO3*\ \&\ SunDur\ \&G}$) using satellite TCO_3 and typical characteristics of clouds (sunshine duration, global solar irradiance), which are measured at numerous weather stations, suggest that it will be possible to reconstruct and trust in the annual ERE over a larger area surrounding Belsk.

6 Conclusions

This paper proposes a method to reveal the sources of long-term variability and the strength of the induced UVR variability due to individual forcing factors. The linear and non-linear superposition of clear sky and cloud effects are also calculated and compared with each other and with observations. The annual erythemal exposure in Belsk in the last decade of the 1976−2023 measurements is about 15% higher than in the first decade. Monthly erythemal exposure during the warm season (April−September) shows a similar increase. No further increase in UVR over central Europe is expected, as theThe positive UVR trend in the 1980s and 1990s was a specific superposition of stratospheric ozone, aerosol and cloud effects. However, from a public health perspective, the small but statistically significant upward trend in seasonal (June−August) UVR exposure at Belsk since about 2000 seems to be of particular interest, as people spend more time outdoors during these summer months. At present, it is difficult to say whether such a trend is due to local effects or whether it is a signal of an emerging non-local, large-scale UVR forcing, probably related to climate change, with a greater frequency of days with cloudless skies. A method is proposed to build a set of models (such as the non-linear GPR models in Section 4.2.1) to investigate sources of long-term variability in ERE, with indices to quantify the influence of selected factors on UVR and the strength of interactions between them. These indices can be applied to any model and set of variables explaining ERE variability.

Author Contribution. Conceptualisation, AC and JK; methodology, AC, JK, JJ, PS, and AP; validation, AC and JK; visualisation, AC; writing (original draft preparation), AC and JK; writing (review and editing), AC, JK, and PS; funding acquisition, JJ and AP. All authors have read and agreed to the published version of the paper.

Competing interests. The contact author has declared that none of the authors has any competing interests.

Acknowledgements. This work was partially financiallyfinanced by the Chief Inspectorate of Environment Protection, contract number GIOŚ/31/2023/DMŚ/NFOŚ. The authors acknowledge ACTRIS research infrastructure for providing aerosol data. Operation of the Polish part of the aforementioned research infrastructure has received financial support from the Minister

of Science, as outlined in agreement no. 2024/WK/04. The authors would also like to thank the DeepL tool (https://www.deepl.com/) for its help in improving the English language.

References

AERONET: Aerosol Robotic Network: https://aeronet.gsfc.nasa.gov/, last access: 19 February 2025.

515 Aun, M., Eerme, K., Ansko, I., & Aun, M.: Daily, seasonal, and annual characteristics of UV radiation and its influencing factors in Tõravere, Estonia, 2004–2016, Theor. Appl. Climatol., 138(1–2), 887–897, https://doi.org/10.1007/s00704-019-02865-1, 2019.

Berger, D. S.: The Sunburning Ultraviolet Meter: Design and Performance, Photochem. Photobiol., 24, 587–593, https://doi.org/10.1111/j.1751-1097.1976.tb06877.x, 1976.

520 Bernard, J., Gallo, R., and Krutmann, J.: Photoimmunology: how ultraviolet radiation affects the immune system, Nat. Rev. Immunol., 19, https://doi.org/10.1038/s41577-019-0185-9, 2019.

Bernhard, G.H., Bais, A.F., Aucamp, P.J., Klekociuk, A.R., Liley, J.B., and McKenzie, R.L.: Stratospheric ozone, UV radiation, and climate interactions, Photochem. Photobiol. Sci., 22(5), 937–989, https://doi.org/10.1007/s43630-023-00371-y, 2023.

525 Bilbao, J., Román, R., de Miguel, A., Mateos, D: Long-term solar erythemal UV irradiance data reconstruction in Spain using a semiempirical method, J. Geophys. Res. Atmos., 116, https://doi.org/10.1029/2011JD015836, 2011.

Borkowski, J.L.: Modelling of UV radiation at different time scales, Ann. Geophys., 26, 3, 441–446, https://doi.org/10.5194/angeo-26-441-2008, 2008.

Calbó, J., Pagès, D. and González, J.-A.: Empirical studies of cloud effects on UV radiation: A review, Rev. Geophys., 43, 530 RG2002, https://doi.org/10.1029/2004RG000155, 2005.

Chadyšiene, R., Girgždys, A.: Ultraviolet radiation albedo of natural surfaces, J. Environ. Eng. Landsc., 16:2, 83-88, https://doi.org/10.3846/1648-6897.2008.16.83-88, 2008.

CIE (Commission Internationale de l'Eclairage): Erythema Reference Action Spectrum and Standard Erythema Dose, CIE 17166:2019, https://www.iso.org/standard/74167.html (last access 15 April 2025), 2019.

535 Čížková, K., Láska, K., Metelka, L., and Staněk, M.: Reconstruction and analysis of erythemal UV radiation time series from Hradec Králové (Czech Republic) over the past 50 years, Atmos. Chem. Phys., 18, 1805–1818, https://doi.org/10.5194/acp-18-1805-2018, 2018.

Cleveland, W. S.: Robust Locally Weighted Regression and Smoothing Scatterplots, J. Am. Stat. Assoc., 74 (368), 829–836, https://doi.org/10.1080/01621459.1979.10481038, 1979.

540 Chubarova, N. E., Pastukhova, A. S., Galin, V. Y., & Smyshlyaev, S. P.: Long-term variability of UV irradiance in the Moscow region according to measurement and modeling data, Izv. Atmos. Ocean. Phys., 54(2), 139–146. https://doi.org/10.1134/s0001433818020056, 2018.

Czerwińska, A., and Krzyścin, J.: Modeling of Biologically Effective Daily Radiant Exposures over Europe from Space Using SEVIRI Measurements and MERRA-2 Reanalysis, Remote Sens., 16 (20), 3797, https://doi.org/10.3390/rs16203797, 2024.

545   den Outer, P.N., Slaper, H., Kaurola, J., Lindfors, A., Kazantzidis, A., Bais, A.F., Feister, U., Junk, J., Janouch, M., and Josefsson, W.: Reconstructing of erythemal ultraviolet radiation levels in Europe for the past 4 decades, J. Geophys. Res. 115, D10102, https://doi.org/10.1029/2009JD012827, 2010.

DeLuisi, J.: Atmospheric Ultraviolet Radiation Scattering and Absorption. In: Zerefos, C.S., Bais, A.F. (eds) Solar Ultraviolet Radiation. NATO ASI Series, vol 52. Springer, Berlin, Heidelberg, https://doi.org/10.1007/978-3-662-03375-3_5, 1997.

550   ERA5: ERA5 hourly data on single levels from 1940 to present, https://cds.climate.copernicus.eu/datasets/reanalysis-era5-single-levels?tab=overview, last access 19 February 2025.

Farman, J., Gardiner, B., and Shanklin, J.: Large losses of total ozone in Antarctica reveal seasonal ClO_x/NO_x interaction, Nature, 315, 207–210, https://doi.org/10.1038/315207a0, 1985.

Fountoulakis, I., Zerefos, C. S., Bais, A. F., Kapsomenakis, J., Koukouli, M.-E., Ohkawara, N., Fioletov, V., Backer, H. D.,
555   Lakkala, K., Karppinen, T., and Webb, A. R.: Twenty-five years of spectral UV-B measurements over Canada, Europe and Japan: Trends and effects from changes in ozone, aerosols, clouds, and surface reflectivity, Comptes Rendus. Géoscience, 350, 393–402, https://doi.org/10.1016/j.crte.2018.07.011, 2018.

Fountoulakis, I., Diémoz, H., Siani, A-M., Laschewski, G., Filippa, G., Arola, A., Bais, A.F., De Backer, H., Lakkala, K., Webb, A.R., De Bock, V., Karppinen, T., Garane, K. Kapsomenakis, J., Koukoul, M-E, and Christos S. Zerefos, C.S.: Solar
560   UV Irradiance in a Changing Climate: Trends in Europe and the Significance of Spectral Monitoring in Italy, Environments, 7(1), 1, https://doi.org/10.3390/environments7010001, 2020.

Fountoulakis, I., Diémoz, H., Siani, A. M., di Sarra, A., Meloni, D., and Sferlazzo, D. M.: Variability and trends in surface solar spectral ultraviolet irradiance in Italy: on the influence of geopotential height and lower-stratospheric ozone, Atmos. Chem. Phys., 21, 18689–18705, https://doi.org/10.5194/acp-21-18689-2021, 2021.

565   GMAO: Global Modeling and Assimilation Office, MERRA-2 tavg1_2d_rad_Nx: 2d,1-Hourly, Time-Averaged, Single-Level, Assimilation, Radiation Diagnostics V5.12.4, Greenbelt, MD, USA, Goddard Earth Sciences Data and Information Services Center (GES DISC), https://doi.org/10.5067/Q9QMY5PBNV1T, last access 19 February 2025.

Holick, M. F. and Chen, T. C.: Vitamin D deficiency: a worldwide problem with health consequences, Am. J. Clin. Nutr., 87, 1080S–6S, https://doi.org/10.1093/ajcn/87.4.1080S, 2008.

570   Juzeniene, A. and Moan, J.: Beneficial effects of UV radiation other than via vitamin D production, Dermato-Endocrinology, 4, 109–117, https://doi.org/10.4161/derm.20013, 2012.

Krzyścin, J. W., and Puchalski, S.: Aerosol impact on the surface UV radiation from the ground-based measurements taken at Belsk, Poland, 1980–1996, J. Geophys. Res., 103 (D13), 16175–16181, 1998.

Krzyścin, J. W., Sobolewski, P. S., Jarosławski, J., Podgórski, J., and Rajewska-Więch, B.: Erythemal UV observations at
575   Belsk, Poland, in the period 1976–2008: Data homogenization, climatology, and trends, Acta Geophys., 59, 155–182, https://doi.org/10.2478/s11600-010-0036-3, 2011.

Krzyścin, J. W.: Biologically effective solar radiation (daily radiant exposure and irradiance at noon) at Belsk from 1 January 1976 to 31 December 2023 based on homogenised measurements with broadband radiometers, IG PAS [dataset], https://doi.org/10.25171/InstGeoph_PAS_IGData_Biologically_Effective_Solar_Radiation_Belsk_1976_2023, 2024.

580   Krzyścin, J., Czerwińska, A., Rajewska-Więch, B., Jarosławski, J., Sobolewski, P.S., Pawlak, I.: Biologically effective radiant exposure for erythema appearance, previtamin D3 synthesis and clearing of psoriatic lesions from erythema biometers at Belsk, Poland, for the period 1976-2023, Earth Syst. Sci. Data Discuss. [preprint], https://doi.org/10.5194/essd-2024-622, in review, 2025.

Lorenz, S., Heinzl, F., Bauer, S., Janßen, M., De Bock, V., Mangold, A., Scholz-Kreisel, P., and Weiskopf, D.: Increasing solar UV radiation in Dortmund, Germany: data and trend analyses and comparison to Uccle, Belgium, Photochem Photobiol Sci, 23, 2173–2199, https://doi.org/10.1007/s43630-024-00658-8, 2024.

Madronich, S.: The atmosphere and UV-B radiation at ground level, in Environmental UV Photobiology, Young, A.; Björn, L.; Moan, J.; Nultsch, W. (eds.). Plenum Press, New York, 1−39, 1993.

Malinović-Milićević, S., Radovanović, M. M., Mijatović, Z., and Petrović, M. D.: Reconstruction and variability of high daily erythemal ultraviolet doses and relationship with total ozone, cloud cover, and albedo in Novi Sad (Serbia), Intl Journal of Climatology, 42, 9088–9100, https://doi.org/10.1002/joc.7803, 2022.

Molina, M. J., and Rowland, F. S.: Stratospheric sink for chlorofluoromethanes: chlorine atom-catalyzed destruction of ozone, Nature, 249, 810–812, https://doi.org/10.1038/249810a0, 1974.

NDACC, Network for the Detection of Atmospheric Composition Change, https://www-air.larc.nasa.gov/missions/ndacc/, last access: 2 July 2025.

Neale, R. E., Lucas, R. M., Byrne, S. N., Hollestein, L., Rhodes, L. E., Yazar, S., Young, A. R., Berwick, M., Ireland, R. A., and Olsen, C. M.: The effects of exposure to solar radiation on human health, Photochem. Photobiol. Sci., 22, 1011–1047, https://doi.org/10.1007/s43630-023-00375-8, 2023.

Posyniak, M., Szkop, A., Pietruczuk, A., Podgórski J., and Krzyścin, J.: The long-term (1964-2014) variability of aerosol optical thickness and its impact on solar irradiance based on the data taken at Belsk, Poland, Acta Geophys., 64, 1858–1874, https://doi.org/10.1515/acgeo-2016-0026, 2016.

Schmalwieser, A. W., Gröbner, J., Blumthaler, M., Klotz, B., De Backer, H., Bolsée, D., Werner, R., Tomsic, D., Metelka, L., Eriksen, P., Jepsen, N., Aun, M., Heikkilä, A., Duprat, T., Sandmann, H., Weiss, T., Bais, A., Toth, Z., Siani, A.-M., Vaccaro, L., Diémoz, H., Grifoni, D., Zipoli, G., Lorenzetto, G., Petkov, B. H., di Sarra, A. G., Massen, F., Yousif, C., Aculinin, A. A., den Outer, P., Svendby, T., Dahlback, A., Johnsen, B., Biszczuk-Jakubowska, J., Krzyscin, J., Henriques, D., Chubarova, N., Kolarž, P., Mijatovic, Z., Groselj, D., Pribullova, A., Gonzales, J. R. M., Bilbao, J., Guerrero, J. M. V., Serrano, A., Andersson, S., Vuilleumier, L., Webb, A., and O'Hagan, J.: UV Index monitoring in Europe, Photochem Photobiol Sci, 16, 1349–1370, https://doi.org/10.1039/c7pp00178a, 2017.

Slaper, H., Reinen, H. A. J. M., Blumthaler, M., Huber, M., and Kuik, F.: Comparing ground-level spectrally resolved solar UV measurements using various instruments: A technique resolving effects of wavelength shift and slit width, Geophysical Research Letters, 22, 2721–2724, https://doi.org/10.1029/95GL02824, 1995.

Solomon, S., Garcia, R. R., Rowland, F. S., and Wuebbles, D. J.: On the depletion of Antarctic ozone, Nature, 321, 755–758, https://doi.org/10.1038/321755a0, 1986.

Trummer, C., Pandis, M., Verheyen, N., Grübler, M., Gaksch, M., Obermayer-Pietsch, B., Tomaschitz, A., Pieber, T., Pilz, S., and Schwetz, V.: Beneficial Effects of UV-Radiation: Vitamin D and beyond, IJERPH, 13, 1028, https://doi.org/10.3390/ijerph13101028, 2016.

TUV: Tropospheric Ultraviolet and Visible (TUV) Radiation Model: https://www2.acom.ucar.edu/modeling/tropospheric-ultraviolet-and-visible-tuv-radiation-model, last access 19 February 2025.

Weatherhead, E. C., Reinsel, G. C., Tiao, G. C., Meng, X., Choi, D., Cheang, W., Keller, T., DeLuisi, J., Wuebbles, D. J., Kerr, J. B., Miller, A. J., Oltmans, S. J., and Frederick, J. E.: Factors affecting the detection of trends: Statistical considerations and applications to environmental data, J. Geophys. Res., 103 (D14), 17149–17161, https://doi.org/10.1029/98JD00995, 1998.

WHO: Global Solar UV Index: a practical guide. A joint recommendation of the World Health Organization, World Meteorological Organization, United Nations Environment Programme, and the International Commission on Non-Ionizing Radiation Protection. WHO, Geneva, Switzerland, 2002.

625 WMO: World Meteorological Organization, UNEP, Report of the Meeting of Experts on UV-B Monitoring and Research, GORMP-No. 03, WMO, Geneva, Switzerland, 1977.

WOUDC: World Ozone and Ultraviolet Radiation Data Centre, https://woudc.org/data.php, last access 2 July 2025.

van der A, R. J., Allaart, M. A. F., and Eskes, H. J.: Extended and refined multi sensor reanalysis of total ozone for the period 1970–2012, Atmos. Meas. Tech., 8, 3021–3035, https://doi.org/10.5194/amt-8-3021-2015, 2015.

630 Young, A. R.: Acute effects of UVR on human eyes and skin, Prog Biophys Mol Biol, 92, 80–85, https://doi.org/10.1016/j.pbiomolbio.2006.02.005, 2006.

Zerefos, C. S., Tourpali, K., Eleftheratos, K., Kazadzis, S., Meleti, C., Feister, U., Koskela, T., and Heikkilä, A.: Evidence of a possible turning point in solar UV-B over Canada, Europe and Japan, Atmos. Chem. Phys., 12, 2469–2477, https://doi.org/10.5194/acp-12-2469-2012, 2012.